Ultramicroscopy 232 (2022) 113408

Contents lists available at ScienceDirect

Ultramicroscopy

journal homepage: www.elsevier.com/locate/ultramic

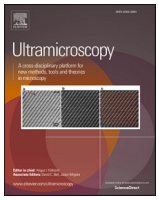

On 2D-FTIR-XRF microscopy – A step forward correlative tissue studies by infrared and hard X-ray radiation

Artur D. Surowka [a,*], Mateusz Czyzycki [a,b,c], Agata Ziomber-Lisiak [d], Alessandro Migliori [c], Magdalena Szczerbowska-Boruchowska [a]

[a] Faculty of Physics and Applied Computer Science, AGH University of Science and Technology, al. A. Mickiewicza 30, Krakow 30-059, Poland
[b] Laboratory for Applications of Synchrotron Radiation, Karlsruhe Institute of Technology, Kaiser Str. 12, Karlsruhe 76131, Germany
[c] Nuclear Science and Instrumentation Laboratory, International Atomic Energy Agency (IAEA) Laboratories, Seibersdorf, Austria
[d] Department of Pathophysiology, Jagiellonian University, Medical College, Czysta 18, Krakow 31-121, Poland

A B S T R A C T

Correlative Fourier Transform Infra-Red (FTIR) and hard X-Ray Fluorescence (XRF) microscopy studies of thin biological samples have recently evolved as complementary methods for biochemical fingerprinting of animal/human tissues. These are seen particularly useful for tracking the mechanisms of neurological diseases, i.e., in Alzheimer/Parkinson disease, in the brain where mishandling of trace metals (Fe, Cu, Zn) seems to be often associated with ongoing damage to molecular components *via*, among others, oxidative/reductive stress neurotoxicity. Despite substantial progress in state-of-the-art detection and data analysis methods, combined FTIR-XRF experiments have never benefited from correlation and co-localization analysis of molecular moieties and chemical elements, respectively. We here propose for the first time a completely novel data analysis pipeline, utilizing the idea of 2D correlation spectrometry for brain tissue analysis. In this paper, we utilized combined benchtop FTIR - synchrotron XRF mapping experiments on thin brain samples mounted on polypropylene membranes. By implementing our recently developed Multiple Linear Regression Multi-Reference (MLR-MR) algorithm, along with advanced image processing, artifact-free 2D FTIR-XRF spectra could be obtained by mitigating the impact of spectral artifacts, such as Etalon fringes and mild scattering Mie-like signatures, in the FTIR data. We demonstrated that the method is a powerful tool for co-localizing and correlating molecular arrangements and chemical elements (and vice versa) using visually attractive 2D correlograms. Moreover, the methods' applicability for fostering the identification of distinct (biological) materials, involving chemical elements and molecular arrangements, is also shown. Taken together, the 2D FTIR-XRF method opens up for new measures for *in-situ* investigating hidden complex biochemical correlations, and yet unraveled mechanisms in a biological sample. This step seems crucial for developing new strategies for facilitating the research on the interaction of metals/nonmetals with organic components. This is particularly important for enhancing our understanding of the diseases associated with metal/nonmetal mishandling.

1. Introduction

Multimodal hyperspectral imaging of biological tissues is an extremely active research area, whose potential technology transfer to the clinical arena is possible due to the opening the possibility to label-free probing and retrieval of biochemically complementary information [1]. This is, in turn, critical to achieve further improves in diagnostic reliability, where existing diagnostic strategies often lack sufficient sensitivity to provide exhaustive information on disease mechanisms when used separately [2]. Multimodal imaging usually takes advantage of a broad range of spectroscopic techniques involving the interaction of analyzed biological materials (i.e., thin slices of soft/hard tissue, body fluids) with electromagnetic radiation (i.e. infrared (IR), visible (VIS), X-ray and/or gamma radiation) and/or ionized particles (i.e. mass spectroscopy (MS)) [3]. Micro-imaging of biological tissues at the cellular level is a particularly vibrant research area that opens up for understanding the complex interplay between cellular signaling and environmentally driven morphological changes [4]. This is particularly important to foster disease modeling to increase our understanding of the pathomechanisms behind uncurable malignancies such as neurologic disorders and cancer [5,6]. Yet the most common studies involve a variety of techniques such as hard/soft X-ray fluorescence (XRF) [7], Fourier Transform Infrared (FTIR) [8], confocal Raman micro-spectroscopy [9] as well as a variety of imaging mass spectrometry tools: time-of-flight secondary ion mass spectrometry (ToF-SIMS) and matrix-assisted laser desorption/ionization (MALDI) [10], among others. Recently, thanks to a multimode metabolomics approach, *Sinclair et al.* showed for the first time that molecular profiling of sebum can be considered as a promising marker for phenotyping of Parkinson disease, as assessed by liquid chromatography mass spectrometry (LC-MS) [11]. *Majzner et al.* presented that bimodal fluorescence and Raman microscopy imaging can provide comprehensive biochemical

* Corresponding author.
E-mail address: asurowka@agh.edu.pl (A.D. Surowka).

https://doi.org/10.1016/j.ultramic.2021.113408
Received 23 June 2021; Received in revised form 14 September 2021; Accepted 3 October 2021
Available online 14 October 2021

information on the fate and trafficking of anthracycline antibiotics at the cellular level [12]. *Lash and Noda* proposed a multimodal analysis using FTIR, Raman, and MALDI-TOF for hyperspectral imaging of molecular arrangements in the brain tissue. The authors showed that the combined approach fosters interpretation of structure and composition spectra [13].

XRF and FTIR microscopy techniques are currently considered popular choices for fast and label-free complementary spectrochemical analysis of chemical elements and molecular arrangements in thin 5–20 μm-thick animal/human tissue samples [14]. There are generally two major experimental layouts for combined FTIR-XRF measurements: (a) semi-parallel (SP): one sample – one method [15] and (b) parallel: one sample – two methods (PA) approaches [16–19]. The former approach, for instance, requires adjacent tissue sections to be investigated: one by FTIR and an adjacent one by XRF. Importantly, this strategy suffers from the natural microscale biochemical variability of tissue slices. In fact, adjacent tissue slices, regardless the thickness, represent distinct projection planes (typically 5–20 μm apart), which tones down the full potential of correlative study [20]. This issue becomes particularly important when fairly constrained histological features, such as amyloid plaques [21,22] and single neurons [23–25], here as selected examples, are a subject of investigation. Their dimensions are often smaller than the sample thickness, and it is hence impossible to assure the investigation of identical features and biochemistry using the adjacent sample strategy. In this regard, the PA approach seems far more attractive. Unfortunately, it requires a coherent sample preparation protocol, involving sample thickness, substrate, and processing, all of which required to achieve a satisfactory signal, and therefore data quality, for both techniques [18,26,27]. What it concerns the sample preparation issue, there are no universally applicable procedures, although attempts are made to standardize the existing approaches [25]. Generally, either hydrated or dehydrated (i.e. freeze-dried samples) tissue samples can be - in principle - applied in combined FTIR-XRF scanning experiments [28]. However, the latter - such cellular cultures in buffer - pose a serious issue as they may require complex water correction procedures in FTIR [29–31] along with the need for the application of cryogenic conditions in XRF to reduce elemental redistribution *via* radiation damage [32]. Needless to mention, due to the time lag between the FTIR and XRF experiments, it becomes practically impossible to assure stable sample storage when measurements are to be done in remote laboratories (such as synchrotron facilities) [33]. In that respect, freeze-dried/lyophilised samples are routinely used, involving soft tissue samples of the brain, heart, and muscle, among others. There is also evidence showing the application of paraffin-embedded soft tissue samples [34], although there is a doubt on the impact of the sample fixatives (i.e., formaldehyde) on the final quantitative information on elemental contents in XRF [25] and molecular profiles (i.e., lipid, protein and carbohydrate) in FTIR experiments [28]. *Bedolla et al.* recently explored radiation damage mechanisms in paraffin-embedded tissue samples on Ultralene films, where the overall radiation damage to distinct molecular components: lipids and proteins, could be triggered by sample fixation protocol [35]. For XRF studies, the sample thickness is usually a complex trade-off between X-ray energy/penetration depth, excitation source/flux (synchrotron facility, benchtop XRF microscope) signal-to-noise ratio, minimal detection limits, sample matrix/density, and, finally, data quantification scheme (i.e., thin and/or intermediate sample approach) if so is needed for chemical elements of interest [36]. We found a brain sample thickness in the range of 15–20 μm (fresh, before drying) sufficient to assure the requirement for negligible self-absorption of primary hard X-rays (10–20 keV) for a range of biologically relevant chemical elements from P to Se [37]. This is a prerequisite for performing the simplest quantification scheme by external standard methods, whereby a priori knowledge on sample organic matrix composition in terms of H, C, N, and O, is not required [38]. What it concerns FTIR, the sample thickness is limited by the penetration depth of mid-IR radiation of approximately 10 μm and the measurement technique: transmission/transflection, so that detector saturation can be avoided. This practically involves the thickness range of 5–10 μm for dried brain samples (ca. 10–20 μm of fresh soft tissue) [38,39].

One of the most important practical issues in FTIR-XRF experiments is the selection of the compatible sample substrate [40]. Recently, polypropylene films and Si_3N_4 membranes emerged as popular choices as XRF-FTIR-compatible substrates due to their optimal absorption figures in the hard X-ray and mid-IR regimes [19,27]. However, the former, commercially known as Ultralene films, were recently found much more problematic for FTIR due to noticeable spatial heterogeneity and the presence of spectral fringing that impact relative band intensities, despite their good durability and optimal size for whole-organ mapping [26]. The latter (Si_3N_4), in turn, despite their higher homogeneity are much more fragile and allow fairly constrained sample areas to be analyzed [40]. Indeed, we have recently highlighted the complexity of this problem in FTIR imaging of brain samples by proposing a new, efficient Multiple Linear Regression Multi-Reference (MLR-MR) algorithm for accounting both spectral fringing and substrate variability issues in FTIR imaging data [41]. However, the radio-resistance of Si_3N_4 membranes to an applied X-ray radiation microprobe should also be taken into account. Though, there is no evidence for any Si_3N_4 damage in the hard X-ray regime, *Surowka et al.* concluded that their exposure to a soft X-ray micro-probe results in reversible multi-interface tissue sample-substrate protonation [42].

Yet the most popular applications of combined XRF-FTIR experiments on biological materials involve the clinical arena. This is seen particularly important for tracking neurodegeneration mechanisms, i.e., in Alzheimer/Parkinson disease, in the brain where mishandling of trace metals (Fe, Cu, Zn) seems to be often associated with ongoing damage to molecular components *via*, among others, oxidative/reductive stress neurotoxicity [43,44]. Somewhat a first combined synchrotron radiation (SR) FTIR and SR- XRF microscopy study by *Leskovjan et al.* took advantage of this correlative approach to shed new light on metal binding mechanisms in amyloid plaques in the Pre-Senilin Amyloid/-Precursor Protein (PS/APP) model of Alzheimer disease. More recently, *Summers et al.* combined FTIR, Raman, XRF, together with classical histological examination to study the distribution patterns of chemical elements and molecular arrangements within/around amyloid deposits of a single 12-month-old transgenic amyloid precursor protein/presenilin-1 (APP/PS1) mouse. Thanks to the applied correlative approach, aggregated protein was found to co-localize to elevated Fe and Zn within the core of a plaque, whilst the levels of lipids, excluding cholesterol, were associated with elevated Cu [44]. *Ducic et al.* coupled multimodal FTIR-XRF along with absorption contrast tomography to study the morphology and composition of myelinated sciatic neurons extracted from wild type mice [45]. Another early account, by *Kastyak et al.*, set out on explaining the formation mechanisms of creatine inclusions in the brain and spinal cord samples of human individuals with Amyotrophic Lateral Sclerosis (ALS). The combined FTIR-XRF methodology allowed to co-localize the deposits to areas where elevated oxidation of lipids (FTIR) was coincided with increased concentrations of trace metals: Fe, Cu and Zn (SR-XRF) [17]. More recently, *Kreuzer et al.*, by using correlative synchrotron XRF and FTIR mapping, confirmed these findings by showing that elevated lipid contents co-localize to oxidized lipids and carbonyl groups in single astrocytes in the hSOD1-G93A animal model of ALS [46].

Another, more recent, applications of this methodology were linked to efficiency studies of new therapies. *Surowka et al.* showed a correlative FTIR-SR-XRF study for investigating the efficacy of new obesity treatments by transcranial direct current brain stimulation (tDCS). This was found sufficient to highlight the action mechanisms of tDCS seem to involve appetite-triggering brain regions where concentration changes of labile action- potential-triggering ions of Na^+, K^+, Ca^{++} were hypothesized to impact lipid fluidity in neural membrane [19]. More recently, *Schriever et al.* confirmed the usefulness of correlative FTIR-XRF studies for dermatology research in defining the fate of tattoo

pigments in the skin. Interestingly, it was shown that the migration of pigment's middle-Z Br and Ti, coincides with an increased abundance of aggregated protein [15]. In addition to purely clinical applications, FTIR-XRF experiments were recently found to address complex practical problems associated with the inherent structural variability of commonly used freeze-dried tissue sections. This is due to the fact that the structural characteristics of a sample - such as mass density - can be accessed in XRF/FTIR either in a quantitative or semiquantitative fashion for the sake of efficient data normalization [16,23,38]. *Leskovjan et al.* took advantage of PA strategy, where FTIR protein signal allowed efficient data normalization for SR-XRF data, and so was sufficient to correct against local mass density variations in the senile plaques and surrounding neuropil area [16].

To date, even though arranged in PA design, combined FTIR-XRF experiments have never benefited from in-depth correlation and co-localization analysis of the observed biochemical patterns between chemical elements and molecular components. The aforementioned studies adapted the correlative approach for visual inspection of imaging/mapping data only, and so was majorly applied to co-localize aberrations in concentrations of chemical elements with that of organic moieties [16,19]. To address this issue, we here propose a novel data analysis pipeline for combined FTIR-XRF mapping experiments, bringing together the idea of 2D synchronous spectrometry, correlation and co-localization analysis [13,47,48]. This approach not only allows to co-localize metal/nonmetal anomalies with those of molecular arrangements, but also opens up for new measures for unraveling hidden complex biochemical correlations in a biological sample. This step seems crucial for developing new strategies for facilitating the *in-situ* research on the interaction of metals/nonmetals with organic components, which is vital for enhancing our understanding of diseases with abnormalities in metal handling pathways, in particular.

2. Materials and methods

2.1. Sample preparation

A single brain specimen ($n = 1$) was extracted from a healthy male Wistar rat, housed in the Department of Pathophysiology, Jagiellonian University Medical College in Krakow, Poland. Then, it was transferred to an ultra-freezer and stored in −80°C until further processing. Just before the FTIR experiments, using a cryo-microtome (−20°C), the specimen was cut into 20 μm -thick serial coronal sections. The sections were instantly mounted onto Ultralene films, the latter fixed/supported between two co-axial Plexiglas rings. For this study, a single slice was selected from a coronal projection plane with overt motor cortex and corpus striatum areas. Finally, the sample was subjected to freeze-drying in a freezer in −80°C. The bioethical permission was obtained from the Local Ethical Committee on Animal Testing at the Jagiellonian University (No. 157/2013). More details on this sample preparation scheme can be found elsewhere [41].

2.2. FTIR microscopy experiments

At first, FTIR microscopy experiments were commenced to avoid data bias due to possible sample degradation *via* radiation damage by a synchrotron hard X-ray microprobe. In doing so, a Thermo Nicolet 8700 FTIR spectrometer (Faculty of Physics and Applied Computer Science, AGH, Krakow, Poland), coupled to a Nicolet Continuum IR Microscope, were used in a transmission mode, involving an 80 × 80 μm aperture (32x condenser/objective) with the step of 100 μm in both directions. The spectral range was constrained to the mid-IR range of 3900–900 cm^{-1} along with the spectral resolution of 6 cm^{-1}. For the interferogram apodization, the Happ-Genzel function was applied. For the background and sample acquisitions, 100 (ca. 60 s) and 30 (ca. 20 s per pixel) scans were co-added. The background was acquired on a clean Ultralene point, located away from the tissue sample.

2.3. SR-XRF microscopy experiments

For assuring high-quality data from a wide range of biologically relevant chemical elements (from phosphorus to zinc), the SR-XRF technique was used. The experiments were completed on the advanced IAEA X-ray spectrometry experimental station installed at Elettra Sincrotrone Trieste (Trieste, Italy) synchrotron facility [49,50]. The experiment took advantage of 10.5 keV synchrotron radiation, monochromatized by a pair of Si(111) crystals with a resolving power of $1.4 \bullet 10^{-4}$. The primary exciting rectangular 200 μm (h) × 100 μm (v) X-ray beam was shaped using a pair of exit slits. The whole setup operated under vacuum ($p = 10^{-7}$ mbar). The resultant beam flux was of ca. $1.7 \bullet 10^{9}$ s^{-1}, as measured upstream sample position. The SR-XRF spectra were acquired by mesh-scanning of the entire coronal section (ca. 16 mm^2) with 4 s exposure time. The spectra were collected using a Bruker XFlash Si drift detector with an energy resolution of 131 eV (for Mn-Kα line) equipped with a Super Light Element Window (SLEW) for allowing detection of low-energy X-rays. For this setup configuration, no overt (visual) signs of radiation damage were concluded, although the sample was exposed to a highly brilliant hard X-ray microprobe, yielding a dose of ca. ~ 10 Gy per pixel (ca. 1 kGy in total) [18].

2.4. Horizontal attenuated total reflectance (HATR) experiments

HATR-FTIR experiments were performed in Faculty of Physics and Applied Computer Science, AGH, Krakow, Poland, to measure the reference FTIR data for fostering the interpretation of FTIR correlograms. These included powdered samples of phosphatydylocholine (Avanti PolarLipids), soy bean phosphatydyloserine (Avanti PolarLipids), and deoxyribonucleic acid (Serva). The spectra were acquired using Thermo Nicolet 8700 FTIR spectrometer equipped with a 10-bounce ZnSe Smart ARK™ High-Energy Throughput Multi-Bounce HATR accessory (Thermo Fisher Scientific). Both 128 and 64 spectra were recorded for the background and sample acquisitions, respectively. The data were recorded in the mid-IR 3900–900 cm^{-1} spectral range, involving a DLaTGS detector with a KBr window. The spectral resolution was set to 4 cm^{-1}. Herein, samples were analyzed by depositing and smearing ca. 0.01 g samples directly onto the clean crystal surface. The acquired spectra can be found in Supplementary Material (SM) in Fig. S1.

2.5. Pre-processing of hyperspectral imaging data

For the whole study, the data preprocessing was kept minimal to yield optimally pristine spectroscopic datasets. The only preprocessing involved the FTIR data, where the spectra were found to be obscured by intense fringing patterns due to inherent IR back-reflections at the Ultralene-air and, to a lesser extent, tissue-air interfaces (cf. Fig. S2). Moreover, due to the variation in Ultralene thickness under the tissue sample, Ultralene contribution to the data had to be compensated to remove its contribution from the points of either higher or lower substrate thickness, as we recently assessed in [41]. This involved the application of our recently developed MLR-MR algorithm [41]. For this procedure, four ($n = 4$) reference spectra, along with the one of Ultralene, were found sufficient to account all spectro-chemical data variability within the scanned tissue area. The output of the MLR-MR procedure can be found in Fig. S2. As can be appreciated from Fig. S2a, showing the distribution of fitted contribution coefficients of Ultralene film in the FTIR spectra, one can see that the membrane contribution to a FTIR spectrum throughout the tissue sample was not homogenous, further justifying the need for the MLR-MR data treatment. It can be drawn from Fig. S2b that the correction yielded data devoid of weak uncompensated Ultralene marker bands at 2990 cm^{-1} and 1380 cm^{-1}.

2.6. Image alignment procedure

First, from the FTIR and XRF images, two maps representing total integrated absorbance ($f_{2r}(x,y)$) and potassium ($f_{1r}(x,y)$) distributions were extracted. Since these maps were of distinct shapes, the latter was subjected to bicubic image interpolation (using the Python's CV library) to match the shape of the former. This was justified by the fact that XRF maps were acquired with the smaller step size in the vertical dimension, and to avoid the losing/binning of higher resolution in $f_{2r}(x, y)$ mesh, it was used as a reference (a static image) for $f_{1r}(x, y)$ (a moving image). Having the $f_{1r}(x, y)$ and $f_{2r}(x, y)$ images of matching size, the image registration was applied to correct against subtle differences in sample orientation during FTIR and XRF experiments. Generally, image registration methods can be divided into spatial vs. frequency domain methods. The former involve operations in the image domain with a lot of open-source packages offering a variety of spatial-domain algorithms i.e. affine transform solutions, be it the DIPY package as an excellent option to be considered [51]. The frequency domain algorithms, in turn, work in the transformed domain. Herein, the Fast Fourier Transform (FFT) based algorithm was exploited, as described by *Reddy and Chatterji* [52]. We have previously found this procedure practically and computationally efficient in aligning XRF and X-ray phase contrast imaging images of the substantia nigra tissue [23]. The procedure's simplicity, computational performance and resilience to noise is due to the Fourier shift theorem, yielding the 2D Fourier transforms of the $f_{1r}(x, y)$ and $f_{2r}(x, y)$ datasets: $F_{1r}(\xi,\eta)$, $F_{2r}(\xi,\eta)$ to be simply related by:

$$F_{2r}(\xi,\eta) = e^{-j2\pi(\xi x_0+\eta y_0)} \otimes F_{1r}(\xi,\eta) \quad (1)$$

where: $F_{1r}(\xi,\eta)$, $F_{2r}(\xi,\eta)$ – the respective Fourier transforms of the $f_{1r}(x, y)$ and $f_{2r}(x, y)$; ξ,η – coordinates in the reciprocal space; x_0, y_0 – coordinates of the affine transformation

In a more general case, where the data require an additional scaling of the data, the underlying transform reads:

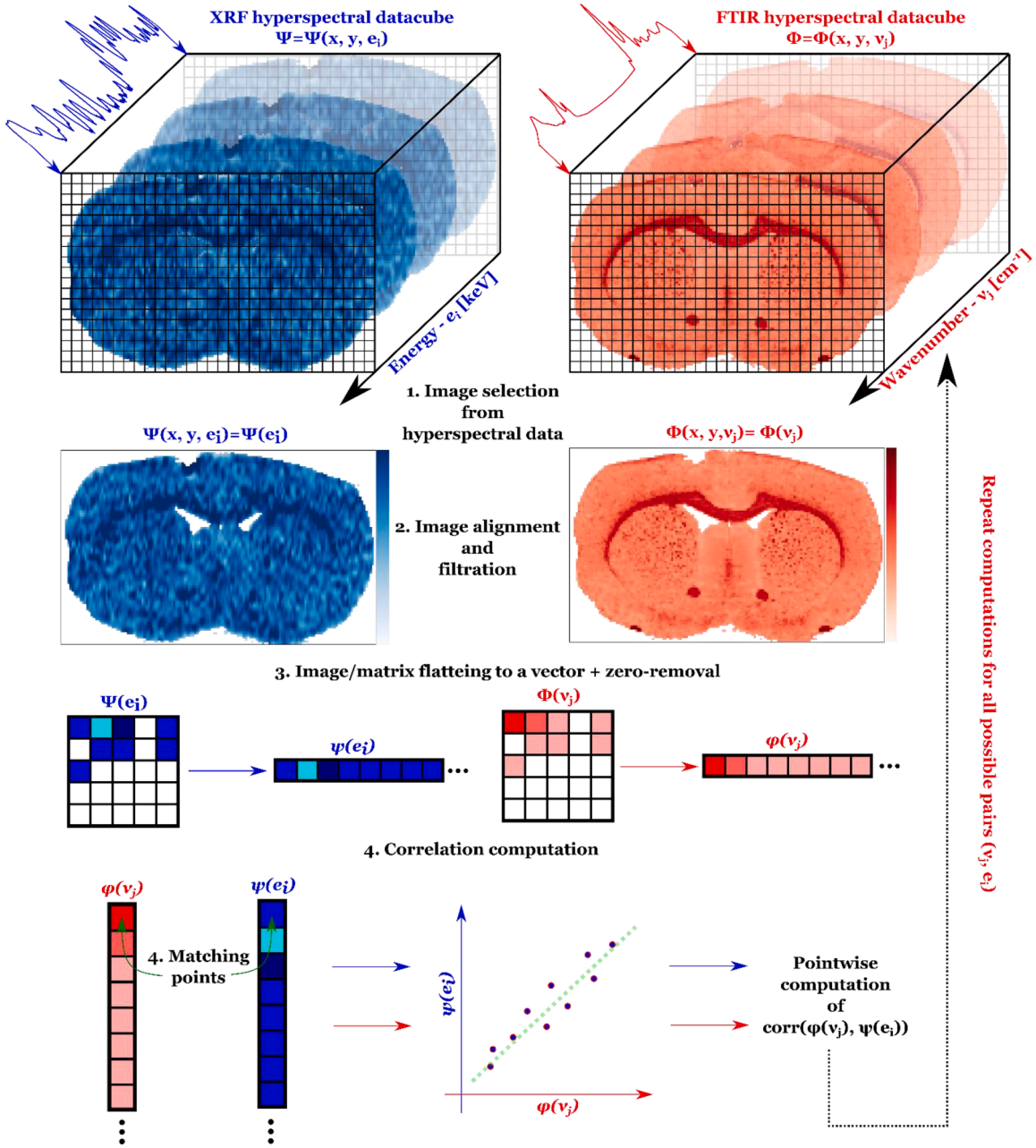

Fig. 1. Layout of the procedure for computation of a 2D-XRF-FTIR spectrum, based on whole sample area.

$$F_{2r}(\xi,\eta) = \frac{1}{|ab|} e^{-j2\pi(\xi x_0+\eta y_0)} \otimes F_{1r}\left(\frac{\xi}{a},\frac{\eta}{b}\right) \quad (2)$$

where: a, b – are scaling factors along ξ,η inverse-domain dimensions, respectively.

In this study, a rotation was also included by translating the data in the Fourier domain. The idea behind the FFT-based algorithm is to estimate the respective parameters (i.e., by the phase correlation technique to include rotation) that yield the registered images to fulfill Eq 1. Herein, to gain in data analysis time, all coordinates of the affine transform: x_0, y_0, a, b were determined for the images $f_{1r}(x,\ y)$ and $f_{2r}(x,\ y)$ only, and were then exploited for transforming the respective single-channel XRF and FTIR datasets. The whole procedure was implemented in Python by using the imreg-dft package (the discrete FT (DFT) registration) [53].

2.7. Computation of a 2D correlation spectrum

To *in-situ* quantify the correlations between molecular components and chemical elements in the brain tissue, we adapted the paradigm of synchronous 2D spectrometry [54]. Recently, this technique is a popular choice for analyzing molecular systems perturbed by external stimuli by spreading, in a channelwise fashion, spectrometric data that are defined by two independent spectral variables. We here proposed a distinct development of this strategy to quantify molecular-elemental correlations in a brain tissue sample [48]. This involves not only channel-wise but also point-wise computations of 2D correlograms, often referred to as synchronous 2D correlation spectra. Herein, the correlation involved two different types of spectra. The whole procedure was outlined in Fig. 1.

Herein, we were dealing with two data cubes that represent 4-dimensional XRF (Ψ) and FTIR (Φ) hyperspectral data cubes (cf. Fig. 1):

$$\Psi = \Psi(x, y, E) \quad (3a)$$

$$\Phi = \Phi(x, y, N) \quad (3b)$$

where: x, y – horizontal and vertical coordinates; E – energy vector of XRF spectra [keV]; N – wavenumber vector of FTIR spectra [cm^{-1}].

XRF and FTIR data cubes represent 4-dimensional matrices, where the first two dimensions are spatial coordinates of an analyzed tissue point (x,y), whereas the last two are the spectral ones. Specifically, the third dimension involves a spectrum collected in x, y. The last 4th dimension represents a specific point in the hyperspectral signal: here, either the absorbance or count number values at specific wavenumber/energy for FTIR and XRF data, respectively.

From these hyperspectral datasets, two 2D spectral maps were selected for specific energy (e_i) and wavenumber (ν_j) spectral coordinates:

$$\Psi(e_i) = \Psi(x, y, e_i) \wedge e_i \in E \quad (4a)$$

$$\Phi(\nu_j) = \Phi(x, y, \nu_j) \wedge \nu_j \in N \quad (4b)$$

where: e_i – selected energy (XRF) value [keV]; ν_j - selected wavenumber (FTIR) value [cm^{-1}].

In order for matching spatial coordinate systems for these two 2D datasets, the images were registered using the DFT algorithm as described above:

$$\Psi_R(e_i) = R(\Psi(e_i)) \quad (5a)$$

$$\Phi_R(\nu_j) = R(\Phi(\nu_j)) \quad (5b)$$

where: R – the registration affine transformation; Ψ_R, Φ_R – registered XRF and FTIR datasets.

The registration transformation yielded two 2D datasets with matching coordinate systems, so that identical $x_i,\ y_i$ coordinates pointed exactly the same tissue area in Ψ, Φ datasets/matrices.

$$\Psi_R(x_i,\ y_i) = \Phi_R(x_i,\ y_i) \quad (6)$$

For allowing computation of the correlation coefficient, 2D maps/matrices $\Psi_R(e_i)$ and $\Phi_R(\nu_j)$ were subjected to matrix flattening to transform these 2D matrices to 1D vectors:

$$\psi(e_i) = F(\Psi_R(e_i)) \quad (7a)$$

$$\varphi(\nu_j) = F(\Phi_R(\nu_j)) \quad (7b)$$

where: $F:\ R^{n\ x\ m} \rightarrow R^N$ – the flattening transformation; $\psi(e_i)$, $\varphi(\nu_j)$ – 1D flattened XRF and FTIR vectors; n,m – width and height of the 2D XRF/FTIR images; $N = n \cdot m$ – total number of pixels in a matching XRF/FTIR 2D image.

One should notice that the $\psi(e_i)$, $\varphi(\nu_j)$ vectors are regarded sparse far away the tissue area. Hence, all the pixels that were not representing the tissue sample (null biochemical information) were then removed from the $\psi(e_i)$, $\varphi(\nu_j)$ vectors to gain in the computational time. Given Eq 4-8, the synchronous spectrum point (or just the correlation coefficient $\rho(e_j,\ \nu_i)$ for ν_i and e_j channels) can be defined as a scalar product of $\psi(e_i)$, $\varphi(\nu_j)$ vectors:

$$\rho(e_i,\ \nu_j) = \frac{1}{N-1}\langle\psi(e_i)|\varphi(\nu_j)\rangle = \frac{1}{N-1}\psi(e_i)^T \cdot \varphi(\nu_j) \quad (8)$$

To assure the computed correlations are scaled in the standard [-1, 1] interval, the column $\psi(e_i)$ and $\varphi(\nu_j)$ data were mean-centered and scaled (divided by respective standard deviations) to yield the Pearson correlation coefficient:

$$\rho(e_i,\ \nu_j) = \frac{1}{N-1}\frac{\langle\psi(e_i)|\varphi(\nu_j)\rangle}{\sigma_{\psi(e_i)}\sigma_{\varphi(\nu_j)}} = \frac{1}{N-1}\frac{[\psi(e_i)^T - \overline{\psi(e_i)}]\cdot[\varphi(\nu_j) - \overline{\varphi(\nu_j)}]}{\sigma_{\psi(e_i)}\sigma_{\varphi(\nu_j)}} \quad (9)$$

$$\rho(e_i,\ \nu_j) \in [-1, 1]$$

where: $\overline{\psi(e_i)}$, $\sigma_{\psi(e_i)}$- average and standard deviation of the flattened XRF $\psi(e_i)$ data; $\overline{\varphi(\nu_j)}, \sigma_{\varphi(\nu_j)}$- average and standard deviation of the flattened FTIR $\varphi(\nu_j)$ data.

Hence, all FTIR spectra were cubically interpolated to yield the same number of spectral channels as that of XRF ones. Then, two spectral channels e_i and ν_j were selected from XRF (Ψ) and FTIR (Φ) datasets, yielding 2D distribution maps $\Psi(e_i)$ and $\varphi(\nu_j)$, respectively. Next, the $\Psi(e_i)$ and $\Phi(\nu_j)$ were registered to output coordinate-matching systems: $\Psi_R(e_i)$ and $\Phi_R(\nu_j)$, respectively. Then, the aligned/registered $\Psi_R(e_i)$ and $\Phi_R(\nu_j)$ matrices were flattened to output $\psi(e_i)$ and $\varphi(\nu_j)$ coordinate-matching vectors, respectively. Finally, zero-filtered $\psi(e_i)$ and $\varphi(\nu_j)$ vectors were a subject of correlation computation using Eq 10. At the end, the synchronous/correlation matrix (ref. correlogram) was obtained:

$$P = \bigwedge_{e_i \in E} \bigwedge_{\nu_j \in N} \rho(e_i, \nu_j) \quad (10)$$

The whole procedure was repeated in a loop until all possible combinations of spectral channels were regarded e_i and ν_j. Final correlogram, obtained for the whole tissue sample here analyzed, can be found in Fig. 2.

2.8. Computation of marginal correlation spectra

By using the correlation matrix P (cf. Eq 11), either its single row (FTIR) or column (XRF) can be extracted, as shown in Fig. 2. This projection yields marginal correlation spectra. For example, by selecting a single column from the P matrix, given a specific XRF energy e_i, a marginal FTIR spectrum can be accessed:

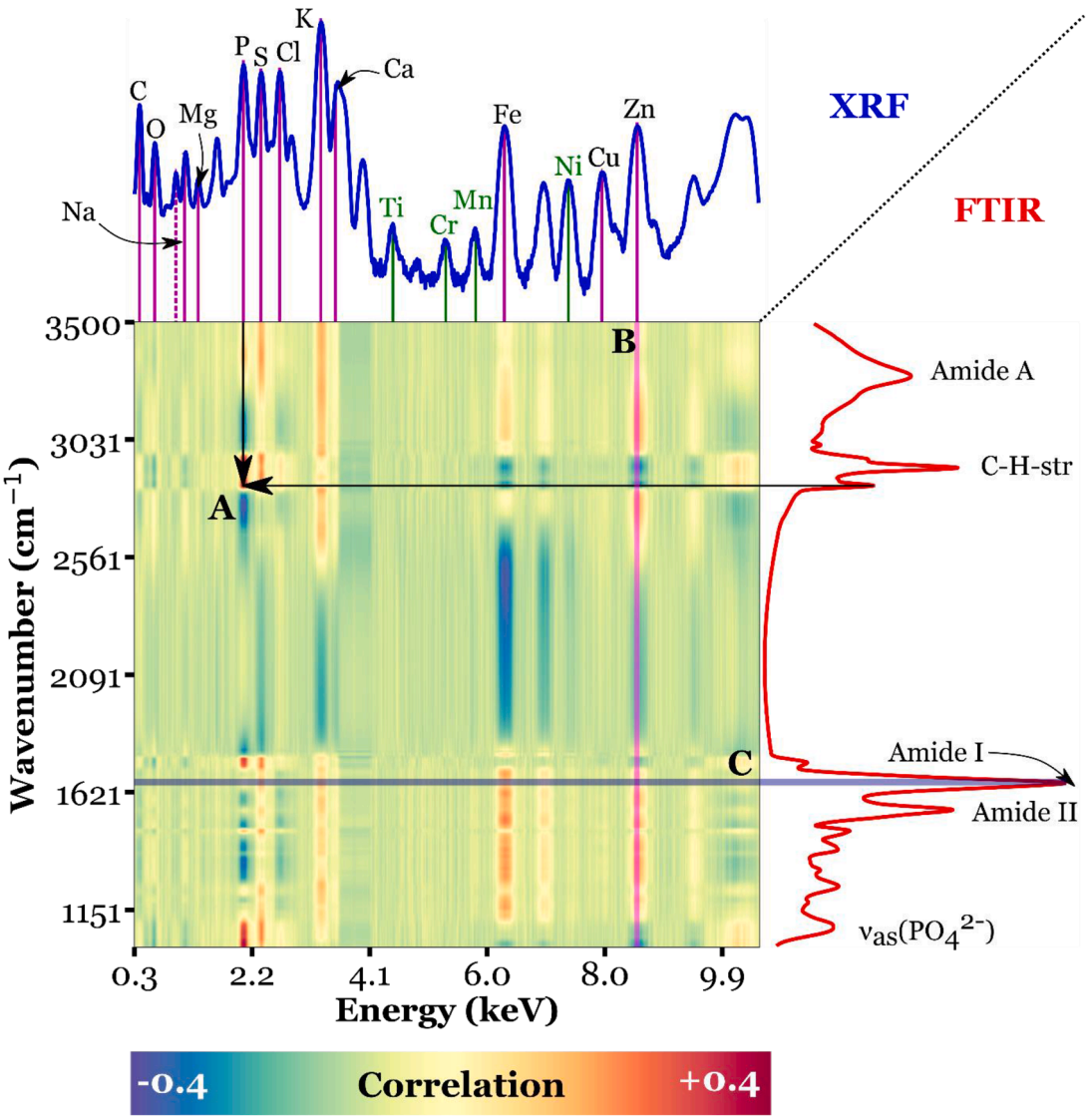

Fig. 2. 2D-XRF-FTIR spectrum for the whole brain sample: A – a point from which a correlation coefficient between P-Kα and CH-str signal was read oud; B – marginal FTIR-Zn spectrum; C – marginal XRF-amide I spectrum. (For interpretation of the references to color in this figure, the reader is referred to the web version of this article.)

$$m_{FTIR}^{e_i} = \mathrm{P}(e_i, N) \tag{11}$$

where: e_i – a selected XRF energy; N – a FTIR wavenumber vector.

In other words, $m_{FTIR}^{e_i}$ shows how specific selected XRF spectral entry (here intensity of a specific fluorescence line/or just a chemical element) is correlated with all chemical bands in an FTIR spectrum: wavenumber by wavenumber. An example $m_{FTIR}^{e_i}(N)$ spectrum was shown in Fig. 2 as trace B, for showing how chemical moieties are correlated with Zn-Kα intensity. Based on Fig. 2, example marginal FTIR spectra were here computed for P-Kα, S-Kα, K-Kα and Fe-Kα signals, as shown in Fig. 3.

Along the same lines, a marginal XRF spectrum can be accessed, given a specific FTIR wavenumber ν_j, by selecting a single row from the P matrix:

$$m_{XRF}^{\nu_j} = \mathrm{P}(E, \nu_j) \tag{12}$$

where: ν_j – selected FTIR wavenumber; E – XRF energies' vector.

Similarly, a marginal spectrum $m_{XRF}^{\nu_j}$ informs how a selected FTIR band coincides with chemical elements in a sample in an energy-by-energy fashion. In Fig. 2 trace C, an $m_{XRF}^{\nu_j}$ spectrum is extracted along amide I (at 1655 cm^{-1}) for demonstrating an association between proteins and chemical elements in an XRF spectrum. Again, based on Fig. 2, exemplary marginal XRF spectra were here computed for aliphatic, lipid ester, protein and phosphate signal, as shown in Fig. 4.

3. Results and discussion

Herein, 2D FTIR-XRF microscopy was applied to unravel and quantify complex molecular and elemental correlations in the coronal brain tissue sample. With the whole experimental setting and data analysis pipeline applied, this proof-of-principle study involves spectrochemical data that provide chemical information on the tissue level involving probing of areas in the order of 10^4 μm^2, averaged over 20 μm thickness. The method outputs 2D FTIR-XRF correlograms (cf. Fig. 2), which can be further subjected to a more careful scrutinization. The output correlograms are expressed in terms of unitless Pearson coefficients within the constrained [-1, +1] range. However, attention should be paid to the elemental concentrations in a sample, so that their levels are sufficient to allow a satisfactory signal to noise in the 2D correlogram. For the sake of comparison, as shown in our previous studies using the same cohort of samples, for example, the concentrations of K were in the range of 5-15 μg/cm^2, Ca within 0.05-0.25 μg/cm^2, Fe within 0.06-0.12 μg/cm^2, Cu

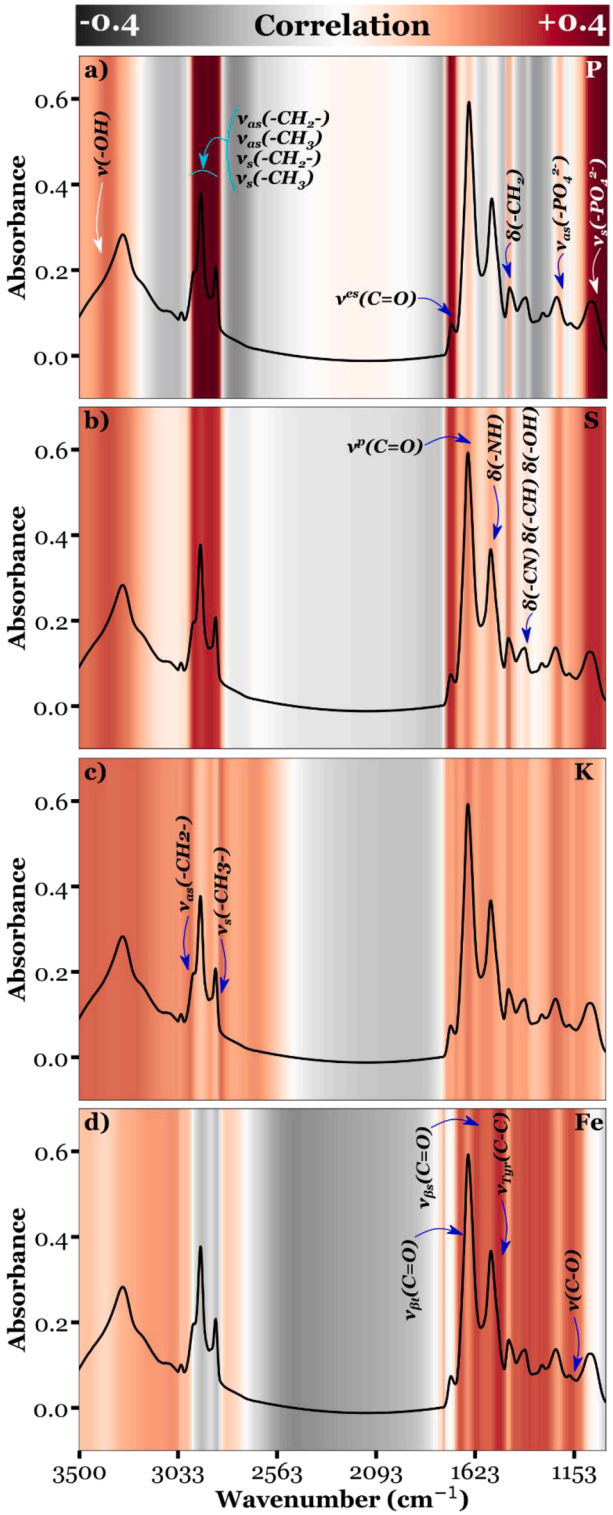

Fig. 3. Marginal FTIR spectra for: (a) P-Kα; (b) S-Kα; (c) K-Kα and (d) Fe-Kα signals.

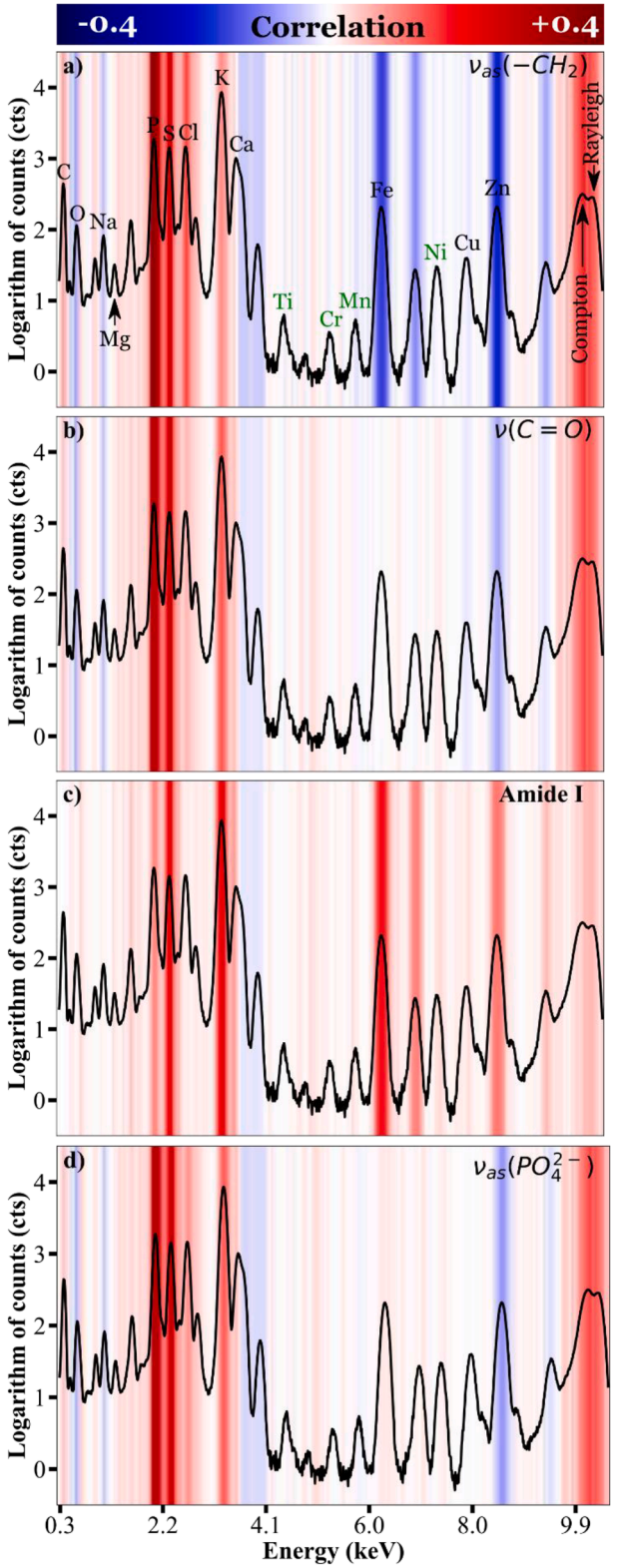

Fig. 4. Marginal XRF spectra for: (a) aliphatic CH-str; (b) lipid ester; (c) amide I and (d) phosphate/phosphodiesters signal.

within 0.005-0.045 μg/cm^2, and Zn 0.02-0.08 μg/cm^2 [19, 55]. By analyzing Fig. 2, one can see that there are vertically constrained positive peaks that are due to correlations of a specific chemical element with molecular arrangements. For the background-like elements: Cr and Ni, the correlation trace is almost zero, which can foster peak assignment in the spectra, by constraining the elements to the investigated biologically relevant ones. As shown in Fig. 2, one should also pay attention to the vertical negative peaks (i.e., for Fe and S) in the vibrationally silent mid-IR spectral range from 1800-2800 cm^{-1}. This seems to be an artifact which can be attributed to the long-range impact of the tails of C-H str (2850-3000 cm^{-1}) and O-H bands (2850-3000 cm^{-1}), both of which elevated in high aliphatic lipid-rich areas. These bands

are, in turn, anticorrelated with the chemical elements that are bound to proteins, such as Fe and S, for which the artifact was noted.

Fig. 2 shows a 2D-FTIR-XRF correlogram, obtained for the whole brain sample analyzed herein (cf. Fig. 1). All correlation values were color-coded, and, for clarity, their contrast was adjusted to span the [-0.4, 0.4] range. The corresponding correlation coefficient between two selected spectral inputs in FTIR and XRF spectra can be obtained from Fig. 2 by reading out the crossing point between two lines originated from two selected input rows/columns. For example, as can be seen in Fig. 2, point A, the correlation coefficient between the phosphorous K_α line (energy 2.0 keV) and $\nu_s(\text{-}CH_3)$ (wavenumber at 2870 cm^{-1}) signal was found to be substantially higher than 0.4, the highest out of all data points. It can be seen from these data that there are even more areas where the correlation coefficients are strong (cf. positive peak - red spots), thus indicating association/colocalization between the respective spectral components in the brain tissue here analyzed. From Fig. 2, a high correlation between phosphorous and aliphatic signals could be generally concluded. To specify all FTIR bands for which the correlation was high, a marginal spectrum can be extracted. By doing so, either a single row or column could be extended from the spectral entries in FTIR/XRF spectra. In Fig. 2 - vertical continuous magenta line B - correlation values between specific FTIR spectral bands and zinc K_α signal intensity was detailed. Similarly, a marginal XRF spectrum can be extracted by selecting a row in the correlation matrix. In Fig. 2, a horizontal continuous violet line C was extended. This represents a single marginal XRF spectrum that shows the correlation coefficients between the intensity lines of chemical elements and amide I intensity (protein signal) at 1655 cm^{-1}.

In Fig. 3a, a FTIR-P-K_α marginal spectrum was color-coded, "smeared" along y-axis, and superimposed on an average FTIR spectrum. From these data, it can be seen that the phosphorous signal coincides with olefins (ca. 3000 cm^{-1}), methyl ($\nu_s(\text{-}CH_3)$ at 2870, $\nu_{as}(CH_3)$ at 2960 cm^{-1}), methylene ($\nu_s(\text{-}CH_2)$ at 2850 cm^{-1}, $\nu_{as}(CH_2)$ at 2920 cm^{-1}, and $\delta(\text{-}CH_2)$ at 2850 cm^{-1}) and lipid ester $\nu(C{=}O)$ at 1730 cm^{-1} vibrational modes, throughout the whole FTIR spectrum. Furthermore, one should note a high correlation between phosphorous and $\nu_{as}(PO_4^{2-})$ and $\nu_s(PO_4^{2-})$ phospholipid/phosphodiester signals at 1240 cm^{-1} and 1046 cm^{-1}, respectively. High association between phosphorous and aliphatic lipid ester osidic residues may follow from phospholipids and phosphodiesters, which are highly abundant in the brain tissue [56]. Neural membranes are particularly enriched with phosphatidylserine and phosphatidylcholine, the latter of the higher abundance [57]. To support this conclusion, the FTIR-P-K_α marginal correlation spectrum was compared with the reference HATR FTIR spectra of phospholipids: phosphatidylcholine, and phosphatidylserine, as shown in Fig S1 (cf. supplementary material). It can be drawn from these data that the FTIR-P-K_α spectrum clearly resembles that of phospholipids: there is a full match between $\nu(=CH)$, $\nu(\text{-}CH_2)$, $\nu(\text{-}CH_3)$, $\delta(\text{-}NH)$, $\delta(\text{-}CH_2)$, $\nu(C{=}O)$ alongside $\nu_{as}(PO_4^{2-})$ and $\nu_s(PO_4^{2-})$ bands, although the intensity of the two latter modes was found to be not properly balanced as compared with the reference spectra here discussed. Nevertheless, the elevated intensity in the 1000-1100 cm^{-1} regime could be easily attributed to the vibrational modes of phosphodiester bonds in DNA/RNA heteropolymers, as presented in Fig. 1S. Hence, taken together, one can infer that the FTIR-P-K_α correlation spectrum may represent a blend of P-containing molecules in the brain.

Fig. 3b shows, in turn, the FTIR-S-K_α spectrum. It can be elaborated from these data that the most prominent marginal correlation peaks were found at peptide-related fingerprint bands: amide I $\nu(C{=}O)$ (ca. 1654 cm^{-1}), amide II $\delta(\text{-}NH_2)$ (ca. 1551 cm^{-1}), as well as $\delta(\text{-}CN)$, $\delta(\text{-}OH)$, and $\delta(\text{-}CH)$ (ca. 1460 cm^{-1}). This can be clearly attributed to sulfur-containing thiols that regulate brain biochemical pathways involving: methylation (i.e. S-adenosyl methionine) [58], antioxidation defense (i.e. glutathione)[59] and cellular signaling (i.e. hydrogen sulfide)[60] reactions, among others. Sulfur correlation/colocalization in protein amide I-II signal can be attributed to disulfide bonds formed in proteins between cystine residues. It should also be noted that brain extracellular matrix collagens are also abundant in sulfur, where disulfide bonds stabilize their triple-helical structure. *Noreen et al.* highlighted that most protein collagen I-IV types' FTIR bands were found at almost the same wavenumbers as here presented in the FTIR-S-K_α spectrum [61].

In contrast to FTIR-P-K_α and FTIR-S-K_α spectra, the FTIR-K-K_α one (cf. Fig. 3c) was found much more uniform, thus suggesting no particular colocalization of potassium to all chemical moieties in the brain tissue here analyzed. Nevertheless, weak correlation peaks were noted for the -CH_2, -CH_3, and PO_4^{2-} moieties. Potassium is a labile metal, participating in electro-chemical current transduction throughout/across the neural membrane [62]. Voltage-gated potassium channels are particularly involved in its handling mechanism [63]. Specifically, this process is regulated by Na^+-K^+-stimulated ATPase [64]. The enzyme is a neural membrane-class protein, bound to aliphatic-rich lipid membranes, underlying potassium transport *via* adenosine triphosphate (ATP) hydrolysis/handling in the brain [64]. These remarks, taken together, can somehow partly highlight that the peak correlations of potassium and phosphodiester/phosphate along with methyl/methylene moieties can be attributed to its colocalization to membrane-bound Na^+-K^+--stimulated-ATPase and ATP, the latter being processed.

As presented in Fig. 3d, FTIR-Fe-K_α marginal correlations were found with peaks in the fingerprint's bands attributed to protein backbone vibrations indicative of β-sheets (1620 cm^{-1}) and β-turns (1670 cm^{-1}) [65]. Interestingly, a positive peak could also be identified for tyrosine ring breathing mode at 1615 cm^{-1} together with a weak one for carbohydrate $\nu(C\text{-}O\text{-}C)$ at 1160 cm^{-1} [66]. Colocalization/binding of Fe and tyrosine residues may draw our attention to tyrosine hydroxylase, which is an ubiquitous pterin-dependent brain enzyme, with Fe^{++} present in its active center [67]. The enzyme catalyzes the process of tyrosine hydroxylation to dihydroxyphenylalanine (DOPA), the latter being an important precursor of common brain catecholamines: norepinephrine, epinephrine and dopamine [68]. This remark can be further supported by the fact that tyrosine hydroxylase has a relatively high contribution of β-sheets and β-turns, as so was confirmed as evidenced by *Martinez et al.*, where a substantial increase of amide I intensity was noted at similar wavenumbers ca. 1620 cm^{-1} and 1670 cm^{-1} [69].

XRF marginal spectra are shown in Fig. 4 for XRF-aliphatic (cf. Fig. 4a), XRF-lipid ester (cf. Fig. 4b), XRF-amide I (cf. Fig. 4c) and XRF-phosphate (cf. Fig. 4d) correlations. It can be seen from Fig. 4a that the aliphatic signal coincided with Kα spectral lines of P, S, Cl, and K. At the same time, the aliphatic arrangements and Fe and, Zn yielded negative correlations. These data support the conclusions made above concerning the colocalization of P, S, Cl, and K with lipid membranes and lipid transporters (cf. Figs. 2-3). At the same time, as shown in Figs. 2 and 3d, all redox-active ions of Fe, Cu, and Zn are co-localized to protein backbones, acting as their cofactors, and hence a negative correlation (here a kind of "competition") could be concluded [55,70]. Along the same lines, XRF-lipid esters (cf. Fig. 4b) along with XRF-phosphate (cf. Fig. 4d) marginal spectra emerged with almost identical profiles, indicating their mutual chemical co-existence, i.e. in brain phospholipids/phosphodiesters, as highlighted above (cf. Fig. 3a and S1). XRF-amide I marginal spectrum, as presented in Fig. 4c, was found with positive peaks for protein-related chemical elements such as S (i.e., thiol bridges), Fe and Zn (enzymes' cofactors), as highlighted above. By analyzing Fig. 4, the Compton and Rayleigh peaks (at ca. 10.5 keV) in XRF marginal spectra could be concluded positively correlated/colocalized to all organic arrangements. Compton/Rayleigh intensity ratio is higher for low-Z elements. Hence, since a brain sample is mostly composed of organic matrix elements: H, C, N, O, accounting more than 90% of the dry mass, its correlation to the organic signal: -CH_2, -CH_3, -C=O, among others, is not surprising [71]. Interestingly, it can be seen from Fig. 2 that the FTIR-Compton trace resembled the FTIR-P- Kα one, and hence it becomes clear that the Compton signal can be mostly due to

the outstanding contribution of lipids/phosphodiesters in the brain tissue.

One single account concerns the local and global character of the proposed 2D-FTIR-XRF spectrometry technique. In general, for more homogenous materials, correlations can be efficiently extracted for the whole sample area. However, in the case of biological samples, distinct anatomo-histological areas exist with various proportions, given a projection plane. This can obscure the most important correlations between chemical elements and molecular components that can be observed in a fairly constrained tissue region. Hence, the most important issue to address at the beginning of the study is to specify a single tissue region that should be subjected to computation. Moreover, one should also note that high resolution spectroscopic (either in terms of spatial and spectral resolution) yield slow computations. Here, by using a personal computer PC (8GB RAM, 2.3 GHz), and given the dimensions of the datasets (FTIR/XRF spectra of 1024 channels and 149×92 pixels in output spectral images) the full computation took around 6 hrs. Hence, one should find a tradeoff between the number of analyzed spectral points and the quality of output 2D-FTIR-XRF correlograms. To address the local sensitivity of the technique to distinct histological areas, brain white and gray matter brain areas were identified and singled out from hyperspectral data, as shown in Fig. 5a-b. Their average XRF and FTIR spectra can be found in Fig S3a-b, respectively. It could be seen in Fig. 5c-d that these areas yielded 2D-FTIR-XRF correlograms with distinct spectrochemical features. Fig. 5c shows a 2D-FTIR-XRF correlogram of the brain white matter. It can be elaborated that these data resemble a phospholipid-like spectrochemical profile due to prominent positive correlation peaks between P-lipid, P-phospholipid, P-lipid ester, S-protein. A weak positive marginal spectrochemical FTIR-Zn profile could also be identified. In fact, the white matter is mostly composed of tracts of myelinated axonal fibers [72]. In addition to phospholipids, myelin is its major chemical constituent. Myelin binds Zn^{++} *via* myelin basic protein (MBP), with phosphate participation, further resulting in protein aggregation and stabilization of myelin sheath [73,74]. A distinct correlogram could be seen for gray matter as shown in Fig. 5d. Positive S-protein, Fe-protein, Cu-protein, and Zn-protein correlations could be noted, thus pointing to the protein-like profile of the material. In fact, gray matter is a fundamental component of the brain. It is made of protein-rich neuron bodies, supporting neuropil (dendrites along with unmyelinated fiber tracts) and glial tissue (astrocytic and oligodendroglial cells), among others [75]. By comparing Figs. 5c-d, another interesting remark emerged for the Compton peak. It can be seen that the marginal FTIR-Compton spectrum is of phospholipid-like profile in the white matter, while it is almost zero in the gray matter. This difference emerges from the differences in the scattering properties of these regions that follow from the fact that gray matter is of higher effective atomic number than lipid-like (carbon- and hydrogen-rich) white matter [76]. *Liu et al.* presented that the Compton/Rayleigh intensity ratio in lacrustine sediments was positively correlated with the aliphatic signal in FTIR spectra (2840-2960 cm-1) [77]. Besides, there is very modest evidence showing the correlation of vibrational bands with Compton intensity, and therefore, our present study, to the best of our knowledge,

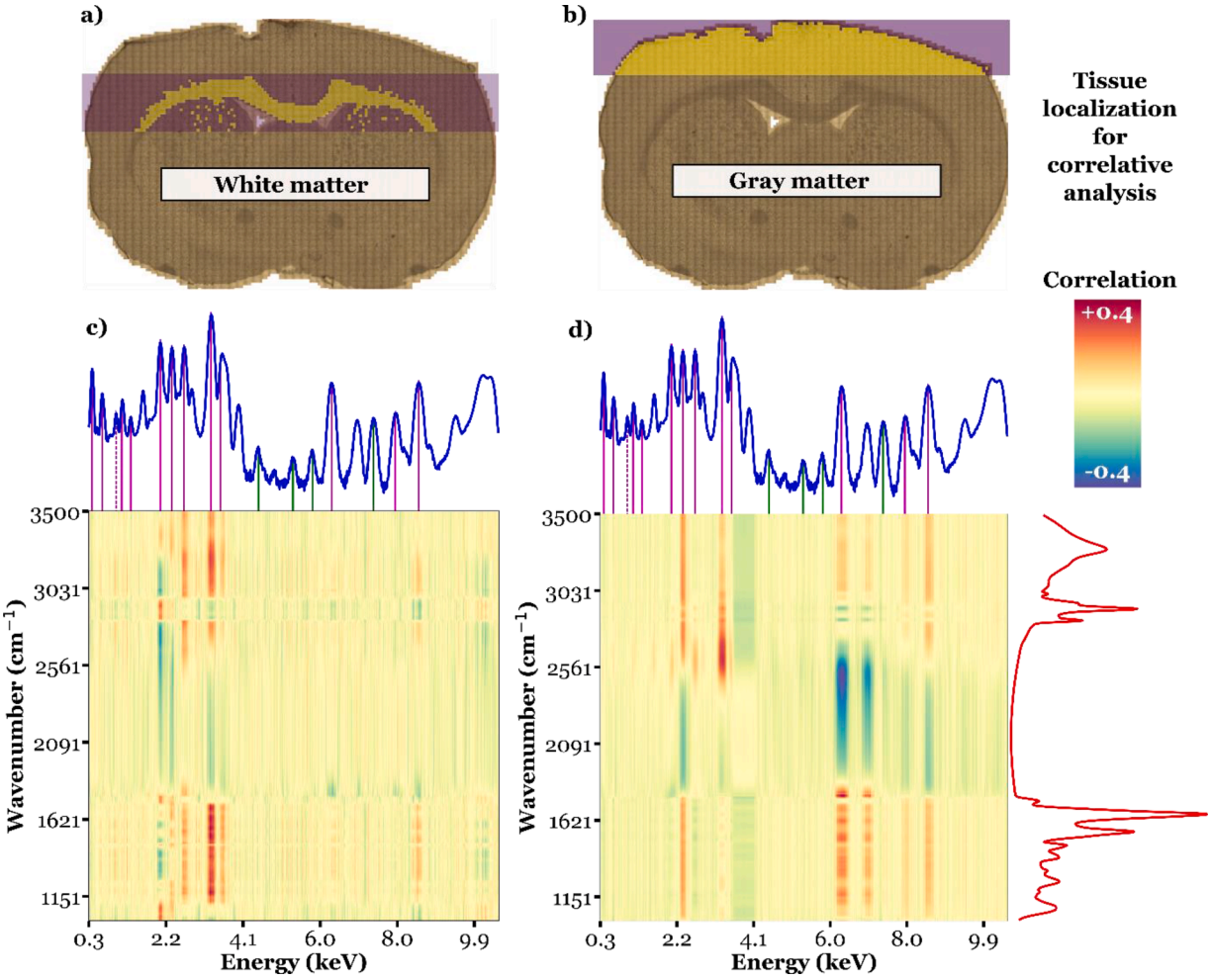

Fig. 5. Data extracted for area-specific correlation analysis are shown in yellow for: (a) white matter; (b) gray matter. 2D-XRF-FTIR spectra for: (c) white matter; (d) gray matter. (For interpretation of the references to color in this figure legend, the reader is referred to the web version of this article.)

is the first systematic account to address this issue comprehensively. Indeed, Fig S3a shows that white matter is of substantially higher Compton signal than gray matter (cf. black arrow in Fig S3a), and its lipid-like aliphatic-rich profile was confirmed in Fig S3b, where substantially increased CH-str and lipid ester C=O signal could be seen (cf. blue arrows in Fig S3b). From Fig S3, it can also be concluded that gray matter is of protein-like profile (cf. Fig S3b), and hence the tissue is enriched with "heavier" organic matrix elements: N and O (cf. Fig S3a), among others, which increases its effective atomic number.

To further strengthen these conclusions, point-wise covariance distribution images were computed to prove that the proposed CH_2, -C=O and -PO_4^{2-} signals are indeed colocalized with the Compton signal in the white matter. In doing so, covariance images $cov_{A,B}$ for every two spectral micro-images: A (the Compton signal from XRF spectra) and B (band heights for $\nu_{as}(CH_2)$ – 2930 cm^{-1}, ν(-C=O) – 1730 cm^{-1}, $\nu_s(PO_4^{2-})$ – 1100 cm^{-1}, amide I – 1650 cm^{-1} and amide II-1550 cm^{-1} signals from FTIR spectra) were calculated as a Hadamard matrix-matrix product:

$$cov_{A,B} = cov_{A,B}(X,Y) = \frac{1}{n}\left(A - \overline{A}\right) \odot \left(B - \overline{B}\right) \tag{13}$$

where: A, B – intensity distributions of specific FTIR and XRF spectral channels; $\overline{A}, \overline{B}$ – average intensity values for A, B images.

In Figs S4a, b, d, f, h, j intensity distributions of Compton (XRF), CH_2, -C=O, -PO_4^{2-}, amide I and amide II signals (FTIR) were presented, respectively. In turn, in Figs S4c, e, g, i and k, the corresponding covariance values were computed between Compton and CH_2, -C=O, -PO_4^{2-}, amide I and amide II signals, respectively. As can be seen from Figs S4c, e and g, the covariance values are indeed elevated within the white matter areas (of the corpus callosum), whilst the covariance with the protein signal, in terms of protein amide I (peptide C=O bonding) and amide II (peptide -N-H bonding), seems to be random throughout the whole sample. This remark further confirms the co-localisation of the elevated Compton scattering intensity mostly to the (phospho) lipid signal, and further shows the advantage of the proposed 2D-FTIR-XRF spectroscopy, and 2D correlograms, for initial screening of the most relevant molecular-elemental correlations.

4. Conclusions

This study demonstrated that 2D-FTIR-XRF microscopy is a new powerful and versatile tool for fostering correlation and co-localization analysis to search for common distribution patterns between molecular arrangements and chemical elements. 2D-FTIR-XRF correlograms here presented enabled more efficient assignment of XRF K_α lines, which enabled robust identification of background elements. The marginal FTIR spectra were shown with substantial chemical interpretability, thus enabling the identification of single molecular arrangements where a considered chemical element exists. This can be a step forward spectral decomposition, which can be exploited for tracking the fate/turnover of chemical elements in biological systems more precisely. 2D-FTIR-XRF correlograms were also demonstrated as a robust tool for enabling the identification of distinct tissue areas – here brain white and gray matter – which can be further extrapolated for the analysis of nontissue materials. Although this study is limited to multimode low-resolution scanning at the tissue level, the method can easily be translated into the field of high-resolution subcellular scanning. At the current state, however, the proposed methodology can be proposed as a departure point for more detailed high-resolution tissue scanning. Noteworthy, the data analysis pipeline here presented can go far beyond the combination of FTIR and XRF techniques, so that other spectral methods can be used to produce 2D correlograms, involving i.e., mass spectrometry imaging. Taken together 2D-FTIR-XRF spectrometry can foster research on metal-protein and metal-lipid interaction and handling, which can facilitate the identification of new complex mechanisms underlying yet uncurable diseases with substantial abnormalities in handling (trace) metals/nonmetals.

Declaration of Competing Interest

The Authors declare no conflict of interests.

Acknowledgements

We would like to thank dr Renata Szymańska for kindly providing phospholipids and DNA for HATR studies. This work was financed by the National Science Centre Poland, grant number DEC-2013/09/B/NZ4/02539 and supported by the International Atomic Energy Agency (IAEA) within the frame of the IAEA Coordinated Research Project No. G42005 as well as by the AGH UST subsidy. The authors make thanks to ELETTRA Synchrotron facility (Trieste, Italy) for the beamtime provision. Research project supported/partly supported by program „Excellence initiative– research university" for the University of Science and Technology.

Supplementary materials

Supplementary material associated with this article can be found, in the online version, at doi:10.1016/j.ultramic.2021.113408.

References

[1] N. Vogler, S. Heuke, T.W. Bocklitz, M. Schmitt, J Popp, Multimodal Imaging Spectroscopy of Tissue, Annu. Rev. Anal. Chem. 8 (2015) 359–387.
[2] J. Gesperger, et al., Improved Diagnostic Imaging of Brain Tumors by Multimodal Microscopy and Deep Learning, Cancers (Basel) 12 (2020) 1806.
[3] W. Ren, et al., Multimodal imaging combining time-domain near-infrared optical tomography and continuous-wave fluorescence molecular tomography, Opt. Express 28 (2020) 9860.
[4] M. Tuck, et al., Multimodal Imaging Based on Vibrational Spectroscopies and Mass Spectrometry Imaging Applied to Biological Tissue: A Multiscale and Multiomics Review, Anal. Chem. 93 (2021) 445–477.
[5] E. Álvarez-Marimon, et al., Synchrotron X-ray Fluorescence and FTIR Signatures for Amyloid Fibrillary and Nonfibrillary Plaques, ACS Chem. Neurosci. 12 (2021) 1961–1971.
[6] K.-Y. Su, W.-L. Lee, Fourier Transform Infrared Spectroscopy as a Cancer Screening and Diagnostic Tool: A Review and Prospects, Cancers (Basel) 12 (2020) 115.
[7] J.F. Collingwood, F Adams, Chemical imaging analysis of the brain with X-ray methods, Spectrochim. Acta - Part B At. Spectrosc. 130 (2017) 101–118.
[8] M.J. Baker, et al., Using Fourier transform IR spectroscopy to analyze biological materials, Nat. Protoc. 9 (2014) 1771–1791.
[9] M. Baranska, Optical spectroscopy and computational methods in biology and medicine, Optical Spectroscopy and Computational Methods in Biology and Medicine (2014), https://doi.org/10.1007/978-94-007-7832-0.
[10] A. Svirkova, A. Turyanskaya, L. Perneczky, C. Streli, M. Marchetti-Deschmann, Multimodal imaging of undecalcified tissue sections by MALDI MS and μXRF, Analyst 143 (2018) 2587–2595.
[11] E. Sinclair, et al., Metabolomics of sebum reveals lipid dysregulation in Parkinson's disease, Nat. Commun. 12 (2021) 1592.
[12] K. Majzner, et al., Nuclear accumulation of anthracyclines in the endothelium studied by bimodal imaging: fluorescence and Raman microscopy, Analyst 140 (2015) 2302–2310.
[13] P. Lasch, I. Noda, Two-Dimensional Correlation Spectroscopy for Multimodal Analysis of FT-IR, Raman, and MALDI-TOF MS Hyperspectral Images with Hamster Brain Tissue, Anal. Chem. 89 (2017) 5008–5016.
[14] C. Petibois, 3D Quantitative Chemical Imaging of Tissues by Spectromics, Trends Biotechnol. 35 (2017) 1194–1207.
[15] I. Schreiver, et al., Synchrotron-based ν-XRF mapping and μ-FTIR microscopy enable to look into the fate and effects of tattoo pigments in human skin, Sci. Rep. 7 (2017) 1–12.
[16] A.C. Leskovjan, A. Lanzirotti, L.M. Miller, Amyloid plaques in PSAPP mice bind less metal than plaques in human Alzheimer's disease, Neuroimage 47 (2009) 1215–1220.
[17] M.Z. Kastyak, et al., Pigmented creatine deposits in Amyotrophic Lateral Sclerosis central nervous system tissues identified by synchrotron Fourier Transform Infrared microspectroscopy and X-ray fluorescence spectromicroscopy, Neuroscience 166 (2010) 1119–1128.
[18] A.D. Surowka, et al., Combined use of infrared and hard X-ray microprobes for spectroscopy-based neuroanatomy, J. Instrum. 13 (2018) C05008.
[19] A.D. Surowka, et al., Molecular and elemental effects underlying the biochemical action of transcranial direct current stimulation (tDCS) in appetite control, Spectrochim. Acta - Part A Mol. Biomol. Spectrosc. 195 (2018) 199–209.

[20] D.M. Simmons, L.W. Swanson, Comparing histological data from different brains: Sources of error and strategies for minimizing them, Brain Res. Rev. 60 (2009) 349–367.
[21] A.D. Surowka, et al., FTIR imaging of the molecular burden around Aβ deposits in an early-stage 3-Tg-APP-PSP1-TAU mouse model of Alzheimer's disease, Analyst 142 (2017) 156–168.
[22] C.R. Liao, et al., Synchrotron FTIR reveals lipid around and within amyloid plaques in transgenic mice and Alzheimer's disease brain, Analyst 138 (2013) 3991.
[23] A.D. Surowka, et al., Combined in-situ imaging of structural organization and elemental composition of substantia nigra neurons in the elderly, Talanta 161 (2016) 368–376.
[24] A.D. Surowka, D. Adamek, E. Radwanska, M. Szczerbowska-Boruchowska, Variability of protein and lipid composition of human subtantia nigra in aging: Fourier transform infrared microspectroscopy study, Neurochem. Int. 76 (2014) 12–22.
[25] J. Chwiej, et al., Preparation of tissue samples for X-ray fluorescence microscopy, Spectrochim. Acta Part B At. Spectrosc. 60 (2005) 1531–1537.
[26] A.D. Surowka, et al., Model-based correction algorithm for Fourier Transform infrared microscopy measurements of complex tissue-substrate systems, Anal. Chim. Acta (2020), https://doi.org/10.1016/j.aca.2019.12.070.
[27] L.M. Miller, et al., A new sample substrate for imaging and correlating organic and trace metal composition in biological cells and tissues, Anal. Bioanal. Chem. 387 (2007) 1705–1715.
[28] V. Zohdi, et al., Importance of Tissue Preparation Methods in FTIR Micro-Spectroscopical Analysis of Biological Tissues: 'Traps for New Users, PLoS One 10 (2015), e0116491.
[29] J. Doherty, et al., Live single cell analysis using synchrotron FTIR microspectroscopy: Development of a simple dynamic flow system for prolonged sample viability, Analyst 144 (2019) 997–1007.
[30] J. Doherty, et al., Increased optical pathlength through aqueous media for the infrared microanalysis of live cells, Anal. Bioanal. Chem. 410 (2018) 5779–5789.
[31] P. Lasch, Spectral pre-processing for biomedical vibrational spectroscopy and microspectroscopic imaging, Chemom. Intell. Lab. Syst. 117 (2012) 100–114.
[32] C. Rumancev, et al., X-ray fluorescence analysis of metal distributions in cryogenic biological samples using large-acceptance-angle SDD detection and continuous scanning at the Hard X-ray Micro/Nano-Probe beamline P06 at PETRA III, J. Synchrotron Radiat. 27 (2020) 60–66.
[33] D.M. Stitt, et al., Tissue acquisition and storage associated oxidation considerations for FTIR microspectroscopic imaging of polyunsaturated fatty acids, Vib. Spectrosc. 60 (2012) 16–22.
[34] D.E. Bedolla, et al., Oxidation of ultralene and paraffin due to radiation damage after exposure to soft X-rays probed by FTIR microspectroscopy and X-ray fluorescence, J. Synchrotron Radiat. 28 (2021) 231–239.
[35] D.E. Bedolla, et al., Effects of soft X-ray radiation damage on paraffin-embedded rat tissues supported on ultralene: a chemical perspective, J. Synchrotron Radiat. 25 (2018) 848–856.
[36] S. Zhou, et al., Elemental assessment of dried and ground samples of leeches via portable X-ray fluorescence, J. Anal. At. Spectrom. 35 (2020) 2573–2581.
[37] M. Szczerbowska-Boruchowska, Sample thickness considerations for quantitative X-ray fluorescence analysis of the soft and skeletal tissues of the human body - theoretical evaluation and experimental validation, X-Ray Spectrom 41 (2012) 328–337.
[38] A.D. Surowka, P. Wrobel, M.M. Marzec, D. Adamek, M. Szczerbowska-Boruchowska, Novel approaches for correction against the soft matrix effects in the quantitative elemental imaging of human substantia nigra tissue using synchrotron X-ray fluorescence, Spectrochim. Acta Part B At. Spectrosc. 123 (2016) 47–58.
[39] K.R. Bambery, et al., Importance of Tissue Preparation Methods in FTIR Micro-Spectroscopical Analysis of Biological Tissues: 'Traps for New Users, PLoS One 10 (2015), e0116491.
[40] E.A. Carter, et al., Silicon nitride as a versatile growth substrate for microspectroscopic imaging and mapping of individual cells, Mol. Biosyst. 6 (2010) 1316.
[41] A.D. Surowka, et al., Model-based correction algorithm for Fourier Transform infrared microscopy measurements of complex tissue-substrate systems, Anal. Chim. Acta 1103 (2020) 143–155.
[42] A.D. Surowka, et al., Soft X-ray induced radiation damage in thin freeze-dried brain samples studied by FTIR microscopy, J. Synchrotron Radiat. 27 (2020) 1218–1226.
[43] A.C. Leskovjan, et al., Increased brain iron coincides with early plaque formation in a mouse model of Alzheimer's disease, Neuroimage 55 (2011) 32–38.
[44] K.L. Summers, et al., A Multimodal Spectroscopic Imaging Method To Characterize the Metal and Macromolecular Content of Proteinaceous Aggregates ('Amyloid Plaques'), Biochemistry 56 (2017) 4107–4116.
[45] T. Dučić, et al., Structure and composition of myelinated axons: A multimodal synchrotron spectro-microscopy study, J. Struct. Biol. 173 (2011) 202–212.
[46] M. Kreuzer, S. Stamenković, S. Chen, P. Andjus, T. Dučić, Lipids status and copper in a single astrocyte of the rat model for amyotrophic lateral sclerosis: Correlative synchrotron-based X-ray and infrared imaging, J. Biophotonics 13 (2020).
[47] T.M. Bauman, E.A. Ricke, S.A. Drew, W. Huang, W.A. Ricke, Quantitation of Protein Expression and Co-localization Using Multiplexed Immuno-histochemical Staining and Multispectral Imaging, J. Vis. Exp. (2016), https://doi.org/10.3791/53837.
[48] I. Noda, Advances in Two-Dimensional Correlation Spectroscopy (2DCOS). Frontiers and Advances in Molecular Spectroscopy, Elsevier, 2018, pp. 47–75, https://doi.org/10.1016/B978-0-12-811220-5.00002-2.
[49] P.M. Wrobel, et al., LabVIEW interface with Tango control system for a multi-technique X-ray spectrometry IAEA beamline end-station at Elettra Sincrotrone Trieste, Nucl. Instruments Methods Phys. Res. Sect. A Accel. Spectrometers, Detect. Assoc. Equip. 833 (2016) 105–109.
[50] A.G. Karydas, et al., An IAEA multi-technique X-ray spectrometry endstation at Elettra Sincrotrone Trieste: benchmarking results and interdisciplinary applications, J. Synchrotron Radiat. 25 (2018) 189–203.
[51] E. Garyfallidis, et al., Dipy, a library for the analysis of diffusion MRI data, Front. Neuroinform. 8 (2014).
[52] B.S. Reddy, B.N. Chatterji, An FFT-based technique for translation, rotation, and scale-invariant image registration, IEEE Trans. Nucl. Sci. 5 (1996) 1266–1271.
[53] Tyc, M. & Gohlke, C. imreg_dft. https://pythonhosted.org/imreg_dft/.
[54] H. Shinzawa, J. Mizukado, S.G Kazarian, Fourier Transform Infrared (FT-IR) Spectroscopic Imaging Analysis of Partially Miscible PMMA–PEG Blends Using Two-Dimensional Disrelation Mapping, Appl. Spectrosc. 71 (2017) 1189–1197.
[55] A. Ziomber, et al., Combined brain Fe, Cu, Zn and neurometabolite analysis – a new methodology for unraveling the efficacy of transcranial direct current stimulation (tDCS) in appetite control, Metallomics 10 (2018) 397–405.
[56] M. Martínez, I Mougan, Fatty Acid Composition of Human Brain Phospholipids During Normal Development, J. Neurochem. 71 (2002) 2528–2533.
[57] H.-Y. Kim, B.X. Huang, A.A. Spector, Phosphatidylserine in the brain: Metabolism and function, Prog. Lipid Res. 56 (2014) 1–18.
[58] J.D. Finkelstein, Metabolic regulatory properties of S-adenosylmethionine and S-adenosylhomocysteine, Clin. Chem. Lab. Med. 45 (2007) 1694–1699.
[59] D. Mendoza-Cózatl, H. Loza-Tavera, A. Hernández-Navarro, R. Moreno-Sánchez, Sulfur assimilation and glutathione metabolism under cadmium stress in yeast, protists and plants, FEMS Microbiol. Rev. 29 (2005) 653–671.
[60] W.-L. Chen, et al., Neuroprotective effects of hydrogen sulfide and the underlying signaling pathways, Rev. Neurosci. 26 (2015) 129–142.
[61] R. Noreen, et al., Detection of collagens in brain tumors based on FTIR imaging and chemometrics, Anal. Bioanal. Chem. 401 (2011) 845–852.
[62] M.J. Pushie, I.J. Pickering, M. Korbas, M.J. Hackett, G.N George, Elemental and chemically specific x-ray fluorescence imaging of biological systems, Chem. Rev. 114 (2014) 8499–8541.
[63] W. Noh, S. Pak, G. Choi, S. Yang, S. Yang, Transient Potassium Channels: Therapeutic Targets for Brain Disorders, Front. Cell. Neurosci. 13 (2019) 265.
[64] M. Habeck, et al., Stimulation, Inhibition, or Stabilization of Na,K-ATPase Caused by Specific Lipid Interactions at Distinct Sites, J. Biol. Chem. 290 (2015) 4829–4842.
[65] A. Barth, Infrared spectroscopy of proteins, Biochim. Biophys. Acta - Bioenerg. 1767 (2007) 1073–1101.
[66] M. Mecozzi, E. Pietrantonio, M. Pietroletti, The roles of carbohydrates, proteins and lipids in the process of aggregation of natural marine organic matter investigated by means of 2D correlation spectroscopy applied to infrared spectra, Spectrochim. Acta Part A Mol. Biomol. Spectrosc. 71 (2009) 1877–1884.
[67] P.A. Frantom, J. Seravalli, S.W. Ragsdale, P.F. Fitzpatrick, Reduction and Oxidation of the Active Site Iron in Tyrosine Hydroxylase: Kinetics and Specificity, Biochemistry 45 (2006) 2372–2379.
[68] J. Opacka-Juffry, D.J.L- Brooks, Dihydroxyphenylalanine and its decarboxylase: New ideas on their neuroregulatory roles, Mov. Disord. 10 (1995) 241–249.
[69] A. Martínez, J. Haavik, T. Flatmark, J.L.R. Arrondo, A Muga, Conformational Properties and Stability of Tyrosine Hydroxylase Studied by Infrared Spectroscopy, J. Biol. Chem. 271 (1996) 19737–19742.
[70] H.-J. Wang, et al., Quantitative imaging of element spatial distribution in the brain section of a mouse model of Alzheimer's disease using synchrotron radiation X-ray fluorescence analysis, J. Anal. At. Spectrom. 25 (2010) 328–333.
[71] A. Ziomber, A.D. Surowka, P. Wrobel, M. Szczerbowska-Boruchowska, Data quantification procedures for a bench-top elemental microimaging of brain specimens for the clinical studies on the obesity treatment by transcranial direct current brain stimulation, X-Ray Spectrom 46 (2017) 388–396.
[72] K.B. Walhovd, H. Johansen-Berg, R.T. Káradóttir, Unraveling the secrets of white matter – Bridging the gap between cellular, animal and human imaging studies, Neuroscience 276 (2014) 2–13.
[73] P. Riccio, et al., Specificity of zinc binding to myelin basic protein, Neurochem. Res. 20 (1995) 1107–1113.
[74] D. Tsang, Y.S. Tsang, W.K. Ho, R.N. Wong, Myelin basic protein is a zinc-binding protein in brain: possible role in myelin compaction, Neurochem. Res. 22 (1997) 811–819.
[75] C.J. Steele, M.M. Chakravarty, Gray-matter structural variability in the human cerebellum: Lobule-specific differences across sex and hemisphere, Neuroimage 170 (2018) 164–173.
[76] H.H. Saleh, J.M. Sharaf, S.B. Alkhateeb, M.S Hamideen, Studies on equivalent atomic number and photon buildup factors for some tissues and phantom materials, Radiat. Phys. Chem. 165 (2019), 108388.
[77] X. Liu, S.M. Colman, E.T. Brown, E.C. Minor, H. Li, Estimation of carbonate, total organic carbon, and biogenic silica content by FTIR and XRF techniques in lacustrine sediments, J. Paleolimnol. 50 (2013) 387–398.